
Article:
Doyle, Scott James, Gibson, Andrew Robert orcid.org/0000-0002-1082-4359, Flatt, Jason et al. (6 more authors) (2018) Spatio-temporal plasma heating mechanisms in a radio-frequency electrothermal microthruster. Plasma sources science & technology. 085011. ISSN 0963-0252

https://doi.org/10.1088/1361-6595/aad79a

Spatio-temporal plasma heating mechanisms in a radio-frequency electrothermal microthruster

Scott J. Doyle[1], Andrew R. Gibson[1], Jason Flatt[1], Teck Seng Ho[2], Rod W. Boswell[2], Christine Charles[2], Peng Tian[3], Mark J. Kushner[3], and James Dedrick[1]

[1]York Plasma Institute, Department of Physics, University of York, Heslington, York, YO10 5DD, UK

[2]Space Plasma, Power and Propulsion Laboratory, Research School of Physics and Engineering, The Australian National University, ACT 0200, Australia

[3]University of Michigan, Dept. of Electrical and Computer Engineering, 1301 Beal Ave., Ann Arbor, MI 48109-2122, USA

[1] E-mail: sjd549@york.ac.uk

July 19, 2018

Abstract

Low power micro-propulsion sources are currently being developed for a variety of space missions. Electrothermal plasma thrusters are of specific interest as they enable spatial control of the power deposition to the propellant gas. Understanding the mechanisms whereby electrical power is coupled to the propellant will allow for optimisation of the heating and fuel efficiencies of electrothermal sources. Previous studies of radio-frequency (rf) plasmas have shown a dependence of the gas and electron heating mechanisms on the local collisionality. This is of particular importance to thrusters due to the large pressure gradients that exist between the inlet and outlet when expanding into vacuum. In this work, phase-resolved optical emission spectroscopy and numerical simulations were employed to study plasma heating in an asymmetric rf (13.56 MHz) electrothermal microthruster operating in argon between 186 - 226 Pa (1.4 - 1.7 Torr) plenum pressure, and between 130 - 450 V (0.2 - 5 W). Three distinct peaks in the phase-resolved Ar($2p_1$) electron impact excitation rate were observed, arising from: sheath collapse heating, sheath expansion heating and heating via secondary electron collisions. These experimental findings were corroborated with the results of 2D fluid/Monte-Carlo simulations performed using the Hybrid Plasma Equipment Model (HPEM). The influence of each mechanism with respect to position within the plasma source during

an α-γ mode transition, where plasma heating is driven via bulk and sheath heating, respectively, was investigated. Sheath dynamics were found to dictate the electron heating at the inlet and outlet, as distinct from the centre of the thruster where interactions of secondary electrons were found to be the dominant electron heating mechanism. Optimisation of the heating mechanisms that contribute to the effective exhaust temperature will directly benefit electrothermal thrusters used on miniaturized satellite platforms.

1 Introduction

Recently there has been a significant interest in the development of compact satellite platforms with on-board propulsion[1–4]. Prospective applications of micro, nano and pico sized platforms (0.1 - 100 kg), such as satellite constellations[5], would benefit from robust, neutralizer-free electric propulsion (EP) sources[6,7]. As such, an increasing percentage of satellites are being equipped with electronically driven propulsion, necessitating the development of compact, low-power, charge-neutral, EP sources for this new generation of satellites[8–11].

Electrothermal plasma microthrusters differ from more traditional resistojets and cold gas thrusters as they enhance the spatial control of the power deposition to the propellant[10,12]. One such source is the Pocket Rocket[13–17], a low power (up to 50 W) asymmetric radio-frequency (rf) capacitively coupled electrothermal microthruster. The thruster is typically powered by a 13.56 MHz rf voltage resulting in a weakly ionized plasma, facilitating the coupling of electrical energy into the propellant[9]. Thrust is produced by the expulsion of hot (1000 K) neutrals, themselves heated via ion-neutral charge exchange collisions, producing a neutral exhaust plume[18]. The thruster and power supply have recently been demonstrated to fit within a standard 1U CubeSat frame, see Ref. 1 for a schematic of the thruster in-situ and Ref. 19 for a schematic of the miniaturized version.

Ions are accelerated radially within the thruster by means of a dc self-bias voltage that forms as a negative surface charge on an insulating alumina dielectric layer, which is located between the plasma and the powered electrode. Time-averaged dc self-biases can arise in capacitively coupled plasmas operating at rf voltages through, for example, a difference in the powered and grounded electrode collecting areas. The dc self-bias voltage forms to balance the time-averaged current reaching each electrode[20]. A negative dc self-bias increases the time averaged voltage drop at the dielectric surface, resulting in greater ion acceleration and, via ion-neutral charge exchange[21], more energetic neutrals exiting the source.

Ions impacting the radial wall can release secondary electrons through the Auger process[22]. These electrons are then accelerated away from the wall back into the plasma through the sheath potential and can reach high energies ($\approx$ 50 eV)[21,23] relative to the ionization potential of the propellant ($\approx$ 14 eV for argon)[15]. Few ions leave the thruster as they are radially accelerated into the radial wall by the dc self-bias voltage and ambipolar forces constrain the electrons. The outlet plume is therefore effectively charge neutral and no external neutralizer is required[13,18]. With no need for an external neutralizer, the size, complexity and power requirements of the Pocket Rocket are reduced relative to other, non-charge neutral, EP sources[8].

The Pocket Rocket is typically operated at relatively high pressures, above 133 Pa (1.0 Torr),

as this represents the Paschen (pressure × distance) minimum for ignition for the relatively small dimensions required by applications in small satellites[24]. The study of high pressure ($\geq$ 1 Torr) rf plasma jets has shown that pressure gradients can greatly affect the plasma heating mechanisms within the source[25]. Electrothermal sources for space propulsion naturally posses a neutral pressure gradient between the gas inlet and the vacuum expansion region, as such the neutral gas and electron heating mechanisms can vary across this region. This effect is compounded as the neutral gas temperature and local ionization fraction are coupled to the local collisionality, leading to a non-linear relationship between axial neutral transport and the effectiveness of plasma heating mechanisms[26–29].

Capacitively coupled rf plasma sources exhibit different electron heating mechanisms depending upon the pressure, applied voltage and geometry. For example, low power discharges are sustained through ionizations during sheath expansion and contraction, and hence show plasma heating at phases of peak temporal voltage modulation (dV/dt)[30]. Sheath collapse heating, e.g field reversal,[31,32] and sheath expansion heating, e.g stochastic,[33,34] occur during phases of peak dV/dt, increasing and decreasing voltage respectively, and are indicative of α-mode operation.

At higher applied voltages, positive ion bombardment onto material surfaces becomes significant, leading to an increased production of secondary electrons, which are subsequently accelerated through the sheath, back into the plasma, reaching maximum energies during full sheath extension[35,36]. These electrons typically have a non-thermal energy distribution and deposit power into the plasma primarily through ionization collisions. Secondary electron heating can be enhanced through the hollow cathode effect (HCE), leading to higher specific power deposition[37,38]. This γ-mode of operation of the Pocket Rocket is desired due to increased neutral gas heating.

Power deposited from ion-neutral charge exchange collisions is highest in the plasma sheaths, where the electric fields couple electrical power into kinetic motion[17,21]. The phase-averaged sheath extent, and hence heated volume of propellant, are related to the local pressure, plasma density and dc self-bias voltage[30]. Therefore, understanding how the phase-resolved electron heating mechanisms link to the phase-averaged sheath dynamics allows for optimization of the neutral gas heating in electrothermal plasma thrusters.

In this work, results from 2D fluid/Monte-Carlo simulations of the Pocket Rocket thruster are compared to experimentally obtained measurements of the phase-resolved Ar($2p_1$) excitation rate. The phase-averaged plasma density, neutral gas heating and spatially resolved power deposition was investigated. Three temporal electron heating mechanisms were identified and the relative changes in excitation from these mechanisms during an α-γ mode transition are presented. Finally, the dominant electron heating mechanism at three axial locations within the thruster are identified and discussed.

The Pocket Rocket source, experimental setup and optical diagnostics are described in section 2. The simulation geometry and computational methods employed are discussed in section 3. Simulated phase-resolved Ar($2p_1$) excitation rates are compared against experimentally measured excitation rates for an argon discharge in α-mode (135 V) and γ-mode (445 V) in section 4. Phase-averaged simulated plasma density, excitation rate and neutral gas temperature are discussed with relation to the dc self-bias voltage and axial power deposition in section 5.1. Three temporal electron heating mechanisms are identified with respect to the phase-resolved dielectric surface voltage in 5.2 and the relative changes in these heating mechanisms with applied voltage are discussed in 5.3. Finally, the spatial extent of each electron heating mechanism is discussed in section 5.4.

2 Experimental Setup

2.1 Description of the Source

The Pocket Rocket source, power coupling circuit and optical configuration are illustrated in figure 1. The thruster consists of an 18 mm long, 4.2 mm inside diameter, 1.0 mm thick, alumina tube through which propellant is passed. A 5 mm long copper electrode is positioned around the midpoint of this tube, supported in a macor housing, and two grounded aluminium rings, of length 4 mm and 2 mm, are positioned around the inlet and the outlet, respectively. The grounded electrodes are separated by 3 mm and 4 mm from the powered electrode on the downstream and upstream sides, respectively. The source was mounted to, and electrically isolated from, an expansion chamber by a 300 mm long Pyrex glass tube. Gas is introduced through a plenum at the upstream side of the source. The pressure was measured by a gauge fitted to the plenum and a Pyrex glass window positioned at the rear of the plenum enabled optical access along the axial length of the source. The source was operated in argon with a plenum pressure of between 186 - 226 Pa (1.4 - 1.7 Torr) and an expansion chamber pressure of 113 Pa (0.85 Torr), matching the experiment.

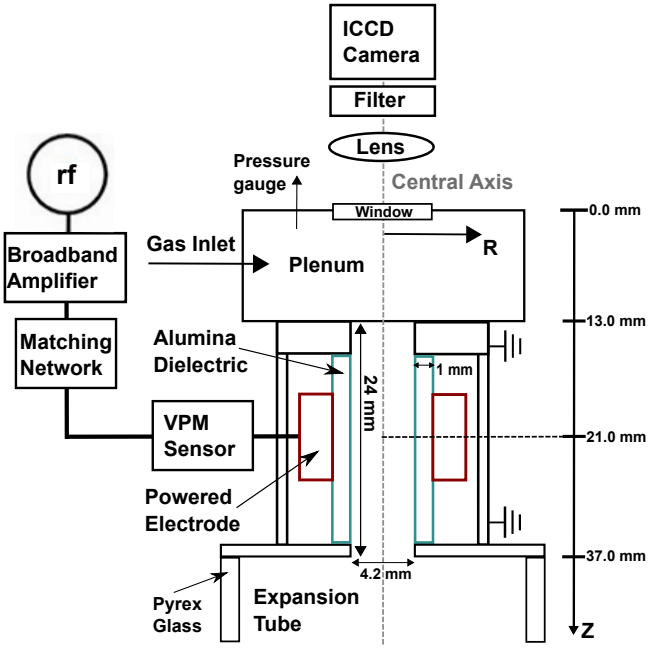

Figure 1: Schematic of the experimental setup (not to scale), showing the power coupling circuit and the orientation of the camera with respect to the plasma source.

The source was operated with a 13.56 MHz driving voltage of between 135 - 445 V amplitude supplied via an external circuit comprising: an arbitrary waveform generator (Keysight 33621A, 120 MHz), broadband amplifier (IFI SCCX100, 0.01 - 220 MHz) and matching network (Coaxial Power Systems MMN150), connected as shown in figure 1. Voltage, current and power were measured with a SOLAYL SAS Vigilant Power Monitor (VPM)[39] and the power deposited into the plasma was obtained via the subtractive method[40,41].

A 1" biconcave lens was positioned in-front of the plenum window which produced an image of the plasma, focused at the midpoint of the alumina tube, shown in figure 1 as a dotted line. Images were recorded by an ICCD camera (Andor iStar DH344T-18U-73, 1024 × 1024 array, pixel size: 13 × 13 μm^2), fitted with a 750.466 nm bandpass filter (LOT-QuantumDesign, 1 nm FWHM), which was positioned at the focal point of the lens. Phase-resolved images were obtained by triggering the camera on the output of arbitrary waveform generator and a digital delay generator (Stanford Research Systems DG645) in series provided a variable delay in the triggering time.

Phase Resolved Optical Emission Spectroscopy (PROES)[42,43] images were taken with an optical gate width of 1.7 ns and a gate step of 2 ns at a sampling frequency of 500 kHz for a total integrated exposure time of 100 ms. As the ICCD camera is aligned axially with the source, the measured optical emission is integrated along the axial line-of-sight within the source. Also, as the plasma is optically thin at the wavelengths of interest, emission from the full length of the source region is able to reach the camera. Therefore, the experimental depth of field (DoF) was taken as 24 mm, equal to the axial length of the source region. To a reasonable approximation, the contribution of the

DoF can be considered flat with respect to axial depth[44]. To replicate a 24 mm DoF in the simulated PROES images, discussed in section 4, the simulated excitation was integrated along the source Z-axis. Radial profiles were taken from the upstream plenum side of the source, the centre of the powered electrode and the expansion region downstream of the source, shown in figure 2 as locations 1, 2 and 3, respectively.

2.2 Electron Impact Excitation Rates

The optical emission from the thruster was measured with respect to time within the rf voltage cycle by PROES. This technique provides information on the dynamics of phase-dependent species in the discharge[43,45]. The optical emission from Ar($2p_1$ - $1s_2$) at 750.4 nm was measured in phase with the driving voltage. This state was chosen as it is dominantly populated from the ground state by direct electron impact excitation[46,47]. The phase resolved optical emission was post-processed to extract the electron impact excitation rate of the Ar($2p_1$) state as summarised below.

The change in population of an excited state n_i at any given time is described by a system of coupled differential equations. These include the electron impact excitation rate from ground to level i, the sum of the excitation rates from metastables to level i, the sum of the cascade contributions due to de-excitation from levels above i and the decay rate from level i as described in equation 1:

$$\frac{\mathrm{d}n_i(t)}{\mathrm{d}t} = n_0 E_{i,0}(t) + \sum_m n_m E_{m,i}(t) + \sum_c A_{ic} n_c(t) - A_i n_i(t) \tag{1}$$

Here, n_0,n_i,n_m and n_c are the ground state, i'th state, metastable state and cascade state populations, respectively. A_i is the Einstein coefficient for state i, A_{ic} is the cascade probability out of state c into state i, while $E_{m,i}(t)$ and $E_{i,0}(t)$ are the electron impact excitation functions for metastable excitation and ground excitation, respectively. Note, that $E_{m,i}(t)$ and $E_{i,0}(t)$ can be obtained from the product of the electron density and the rate coefficient for the relevant process. By assuming that the Ar($2p_1$) excited state is not heavily populated through cascade processes or step-wise (metastable) excitation, the excitation function $\mathrm{E}_{i,0}(t)$ can be equated directly to the number of photons emitted $n_{\mathrm{Ph,i}}(t,r)$ via[43]:

$$E_{i,0}(t) = \frac{1}{n_0 A_{ik}} \left(\frac{\mathrm{d}n_{\mathrm{Ph,i}}(t,r)}{\mathrm{d}t} + \frac{1}{\tau_{\mathrm{eff}}} n_{\mathrm{Ph,i}}(t,r) \right) \tag{2}$$

where the photon flux $n_{\mathrm{Ph,i}}(t,r)$ is given as:

$$n_{\mathrm{Ph,i}}(t,r) = A_{ik} n_i(t,r) \tag{3}$$

Here, $n_i(t,r)$ and A_{ik} are the radial population density and transition probability out of state i, respectively. The effective lifetime of state i is denoted by τ_{eff}, taking into account spontaneous emission and collisional quenching given by:

$$\frac{1}{\tau_{\text{eff}}} = \sum_k A_{ik} g_{ik} + \sum_q k_q n_q \tag{4}$$

Where $g_{ik} = 1$ is the optical escape factor[48,49] and k_q, n_q are the quenching coefficient and density of quenching species q, respectively. In this work quenching is assumed to be performed only by neutral argon where the quenching coefficient ($k_{ar} = 1.6 \times 10^{-17}$ m^3 s^{-1}) is evaluated for a neutral gas temperature of 1000 K[47,50].

3 Description of the Model

3.1 Mesh Geometry and Operating Conditions

Two-dimensional, fluid-kinetic simulations were undertaken using the Hybrid Plasma Equipment Model (HPEM)[51]. The Pocket Rocket mesh geometry is illustrated in figure 2. An external circuit (not shown) comprising: an rf voltage source and blocking capacitor was connected to the powered electrode. Although a blocking capacitor is included within the circuit, the alumina dielectric layer prevents a dc current back to the power source and maintains the time averaged dc self-bias voltage as a negative surface charge.

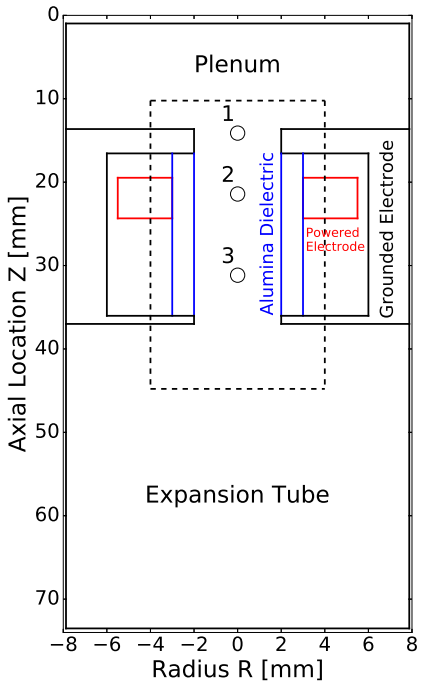

Figure 2: Illustration of the simulation domain (not to scale). The domain is radially symmetric around R = 0.0 mm. Gas is introduced into the plenum and extracted at the end of the expansion tube. An rf voltage is applied to the electrodes, denoted in red, and couples to the plasma through an alumina tube, denoted in blue. The source region, highlighted by dotted lines, contains three sub-regions of interest: upstream (Z = 14.2 mm), the powered electrode (Z = 21 mm) and downstream (Z = 31 mm), regions 1, 2 and 3, respectively.

The numerical mesh consisted of 64 × 152 (R × Z) cells in a cylindrically symmetric geometry, corresponding to a radial resolution of 0.125 mm per cell and an axial resolution of 0.5 mm per cell. A higher radial resolution is required to resolve the electric field gradient through the powered electrode sheaths. The powered electrode was driven by a 13.56 MHz voltage of amplitude 120 - 450 V. The source was operated in argon with an input flow rate of 100 sccm at the gas inlet and a fixed pressure of 0.85 Torr at the outlet, resulting in a plenum pressure of 226 Pa (1.7 Torr) at 445 V, closely matching the experimental setup.

3.2 Simulation Theory

To enable specifying an outlet pressure boundary condition, modifications were required to the model. The simulation is a multi-fluid model in which a momentum equation is solved for each neutral species. In the momentum equation, the momentum flux is solved at the half-points between the mesh points for density and temperature. The procedure to implement the pressure boundary condition is as follows. First, the numerical mesh points corresponding to the face of the pump in contact with the plasma are recorded. The pressure gradient appearing in the momentum equation for each species is between the pump-node and the nearest neighbor plasma nodes. For each species, the densities at the

nearest plasma nodes to the pump node are averaged and placed at the pump face. These collected densities are then used to compute mole fractions. The partial pressure of each species at the pump face is then the mole-fraction of that species multiplied by the outlet pressure boundary condition. The inlet boundary condition is the flow rate, which determines the momentum of each species at the face of the inlet. With the inlet flow rate and pressure at the outlet port specified, the pressure gradient between the two naturally results from the calculation.

The charged particle species included in the simulation are Ar^+, Ar_2^+ and e^-, with the trajectory of electrons released from material surfaces following ion bombardment (secondary electrons) being kinetically tracked using a Monte-Carlo simulation separately from electrons in the plasma bulk. Neutral species included are: Ar, Ar($1s_2$), Ar($1s_3$), Ar($1s_4$), Ar($1s_5$), Ar($4p$), Ar($4d$) and Ar_2^*. Excitation of the Ar($4p$) lumped state is used as a proxy for excitation of Ar($2p_1$) and the full reaction mechanism is as discussed in Ref. 52. An explicit simulation of radiation transport is not included here.

The energy distribution functions of ions and neutrals are assumed to be Maxwellian with a superimposed advective velocity as the plasma is considered to be collisional at 186 - 266 Pa (1.4 - 1.7 Torr) plenum pressure. The energy distribution functions for electrons created in the bulk plasma are obtained from the solution of the two-term approximation of the Boltzmann equation.

Secondary electron emission from the radial walls of the thruster is introduced using an energy independent model, where the secondary electron flux is proportional to the incident ion fluxes and the secondary electron emission coefficient[53]. Secondary electron emission coefficients are set to $\gamma = 0.2$ and $\gamma = 0.0$ at the surface of the alumina wall and outside the plasma source, respectively. Once created, secondary electron pseudo-particles are launched from the material surface with an initial energy of 3 eV and are further accelerated through the local potential gradient, where their motion and collisions are tracked using a Monte-Carlo algorithm[54]. The kinetic treatment of the secondary electrons ensures that, aside from the initial launch energy, there are no further assumptions made regarding the shape of the secondary electron energy distribution.

The density of species N_i within any given cell is determined from the mass continuity between adjacent cells (equation 5).

$$\frac{\delta N_i}{\delta t} = -\nabla \cdot \phi_i + S_i \tag{5}$$

Here, ϕ is the flux of particles between adjacent cells and S_i is the particle source function due to electron impact and heavy particle collisions. For electrons ϕ is accounted for using the drift diffusion approximation implemented using Scharffeter-Gummel fluxes[55]. Reaction rates for the collisional processes are determined from the solution of the two-term Boltzmann equation. In the case of heavy

particle reactions rate coefficients are used in Arrhenius form[51].

For ions and neutrals, the species flux and temperatures are obtained from more complete versions of the momentum and energy continuity equations (equations 6 and 7). Neutral species exclude the terms with the electric fields, while the viscosity terms are not included for ions due to the low density of ions relative to neutral particles.

$$\frac{\delta\phi_i}{\delta t} = -\frac{1}{m_i}\nabla\left(N_i k_b T_i\right) - \nabla\cdot\left(N_i v_i^2\right) + \frac{q_i}{m_i}N_i\mathbf{E} - \nabla\cdot\bar{\bar{v}}_i - \sum_j \frac{m_j}{m_i m_j}N_i N_j\left(v_i - v_j\right)\nu_{ij} \quad (6)$$

Here T_i, m_i and v_i are the mean temperature, mass and velocity of species i, respectively. $\bar{\bar{v}}_i$ is the viscosity tensor for species i, ν_{ij} is the collision rate between species i and j, E is the electric field strength and k_b is Boltzmann's constant. The summation term is performed for each heavy particle species j for which collision rates have been defined. Electron-neutral and electron-ion collisions solved for in the model include elastic, excitation and ionization reactions. As described in Ref. 52, cascade processes, multi-step ionization and heavy particle mixing between excited species are also included, the interaction cross-sections and rate coefficients for which are obtained from Refs. 56–60.

The energy conservation equation (equation 7) allows the computation of the temperature of each species by considering its thermal conductivity κ and the inclusion of a change in enthalpy term. The final term applies a temperature dependency to the collision rates, with rate coefficient k_{ij}, and accounts for ion-neutral charge exchange heating. The general form of the energy continuity equation for heavy particles is written as:

$$\begin{aligned}\frac{\delta N_i c_i T_i}{\delta t} = \nabla\cdot\kappa\nabla T_i - P_i\nabla\cdot v_i - \nabla\cdot\left(N_i v_i \epsilon_i\right) + \frac{N_i q_i^2}{m_i v_i}\mathbf{E}^2 \\ + \sum_j \frac{m_j}{m_i m_j}N_i N_j \nu_{ij} k_b\left(T_j - T_i\right) \pm \sum_j N_i N_j k_{\Delta H_{ij}}\Delta H \pm \sum_j 3 N_i N_j k_{ij} k_b T_j \quad (7)\end{aligned}$$

Where c_i is the specific heat capacity, P_i is the partial pressure and ϵ_i is the specific energy of species i. The change in enthalpy for an exothermic or endothermic reaction is ΔH and the rate coefficient for reactions with a change in enthalpy is given as $k_{\Delta H_{ij}}$. Equation 7 can be extended into solids to provide material temperatures. For material nodes, the only terms on the RHS that are retained are thermal conduction and sources of heat due to ion collisions and surface neutralisation of ions.

Ion-neutral charge exchange collisions are employed with a rate coefficient $k_{ce,ij} = 5.66\times10^{-10}\ \mathrm{cm}^{-3}\ (T_g/300)^{0.5}$ where T_g is the neutral gas temperature[61]. During a symmetric charge exchange collision, the temperatures of the ion and neutral are exchanged, resulting in a significant heating source for neutrals and cooling of the ions. Ions striking the radial alumina wall deposit their kinetic energy and remaining

potential energy after their Auger based neutralisation[21]. As the temperature of the walls increases, conductive heat losses are reduced and the on-axis neutral gas temperature increases (see figure 3).

Thermal energy transport from the neutral gas towards the radial wall is accounted for using the approach described in Ref. 62, based upon a temperature 'jump' across the computational cell adjacent to the surface[63]. This temperature jump is determined largely by the thermal energy accommodation coefficient α_E, which is dependent on a variety of surface conditions, including the neutral gas temperature. In this work a value of $\alpha_E = 0.4$ is applied, which is based on extrapolating the temperature dependence of the thermal energy accommodation coefficient measured by Yamaguchi et al[64] for argon atoms incident on platinum surfaces to a temperature of 1000 K. In general, argon thermal energy accommodation coefficients have been found to be relatively independent of the surface material[65].

3.3 Determining Wall Temperatures

The ion flux incident on the radial wall results in a heating of the wall material. Previous work has shown that wall heating in the Pocket Rocket occurs over relatively long time scales ($\approx$ 100 s)[21]. This cannot be easily accounted for on the typical simulation timescales (100 μs - 10 ms)[51]. To approximate this effect two sets of simulations were performed: one with a fixed initial wall temperature of 325 K and a second with an initial wall temperature derived from a two-step procedure, described below. The maximum on-axis neutral gas temperatures with respect to applied voltage for both sets of simulations are shown in figure 3.

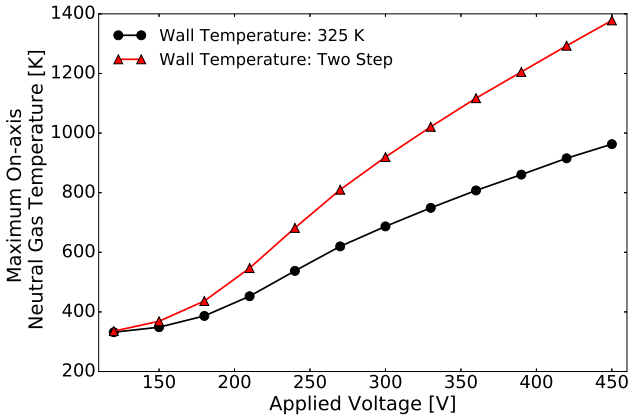

Figure 3: Phase-averaged on-axis (R = 0 mm) neutral gas temperatures with respect to applied voltage with 325 K walls (black circles) and with the wall temperature determined by the two step method (red triangles). Plenum pressure 186 - 226 Pa (1.4 - 1.7 Torr) in argon for 13.56 MHz driving voltage amplitudes between 120 V - 450 V.

The two-step method was performed as follows. In the first step, the maximum on-axis neutral gas temperature was computed using a 'cold' wall at 325 K. In the second step, the simulations were re-run with the wall temperature initialized as the maximum value of neutral gas temperature

determined in the first step. As shown in figure 3 the two step method resulted in higher on-axis neutral gas temperatures, with the difference increasing with applied voltage. The cold wall neutral gas temperatures in figure 3 closely match those previously simulated using the computational fluid dynamics code CFD-ACE+[17,21].

3.4 Determining Collisionality

The neutral gas is primarily heated through ion-neutral charge exchange[21], and hence accurate modelling of the neutral density, and hence collisionality, is important. The collisional regime is described by the Knudsen number[66], K_n, the ratio between the atomic mean free path λ and a characteristic dimension of the system L:

$$K_n = \frac{\lambda}{L} = \frac{1}{N_{Ar}\sigma_{Ar}2R} = \frac{k_B T_g}{PV}\frac{1}{\sigma_{Ar}2R} \tag{8}$$

Here, N_{Ar} is the Ar ground state density, related to the pressure P, neutral gas temperature T_g and discharge volume V by the ideal gas law, σ_{Ar} is the collisional cross-section for collisions between two Ar atoms and R is the radius of the discharge region (2.1 mm, figure 3.1). As the Pocket Rocket operates in the slip-flow transition boundary regime ($0.01 \leq K_n \leq 0.35$)[67], a slip condition[68] was applied to plasma-material boundaries to maintain non-zero fluid velocities at material surfaces[69].

The simulated phase-averaged on-axis Knudsen number for three voltages, 150 V, 300 V, and 450 V is shown in figure 4 where an axial location of zero is at the top of the plenum (See fig 3.1).

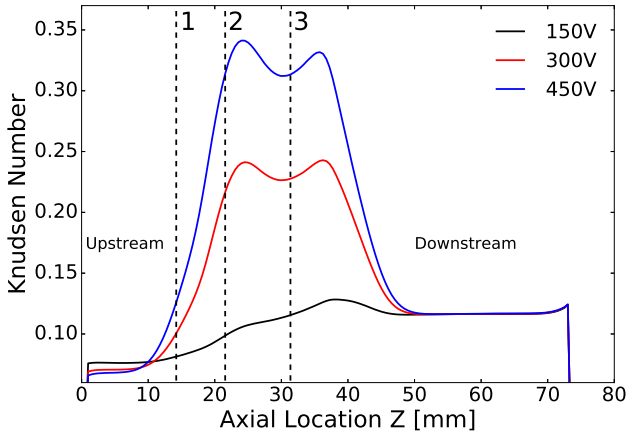

Figure 4: Phase-averaged on-axis profiles the Knudsen number showing a reduced collisionality in the heated region of the source. Plenum pressure 226 Pa (1.7 Torr), driven at 13.56 MHz, 150 V, 300 V and 450 V amplitudes, with 349 K, 687 K, 967 K alumina wall temperatures, respectively. An axial location of zero is at the top of the plenum.

The neutral gas temperature increases with applied voltage and power deposition, resulting in a reduction in neutral density within the source region ($12 \leq$ Z ≤ 38 mm), reducing the collisionality and increasing the Knudsen number. As neutral gas heating is primarily a collisional process, this

feedback between heating and collisionality sets a limit on the achievable heating efficiency. The on-axis Knudsen number profile for 150 V shows close agreement with previous work performed for cold gas operation using CFD-ACE+[16,17].

3.5 Determining Thrust

The simulated thrust F_T was obtained by integrating the ion and neutral mass flux through an axial plane, one cell thick (0.5 mm), at the exit aperture of the thruster (Z = 37mm). The method employed was adapted from Ref 70:

$$F_T = \int_0^R A_c \left(\sum_{k=0}^{n} v_{kn} \dot{m}_{kn} \right) + A_c \left(\sum_{k=0}^{n} v_{ki} \dot{m}_{ki} \right) \mathrm{d}R + \int_0^R A_c \Delta P \mathrm{d}R \tag{9}$$

when considering only neutral Ar and Ar^+ this simplifies to:

$$F_T = \int_0^R A_c (v_{Ar} \dot{m}_{Ar}) + A_c (v_{Ar^+} \dot{m}_{Ar^+}) \mathrm{d}R + \int_0^R A_c \Delta P \mathrm{d}R \tag{10}$$

where R is the radius of the source (2.1 mm), A_c is the cross-sectional area of a simulation cell (in cylindrical coordinates), v_{Ar} and v_{Ar^+} are the neutral Ar and Ar^+ ion velocities respectively. The mass flux rates through the plane of integration are denoted by $\dot{m}_{Ar}$ and $\dot{m}_{Ar^+}$ for Ar and Ar^+, respectively. Here the neutral mass flux rate is defined $\dot{m}_{Ar} = m_{Ar}\Gamma_{Ar}$, for the argon ion mass m_{Ar} and argon flux Γ_{Ar}, the argon ion mass flux rate is defined in the same way for the Ar^+ flux. The differential pressure across the plane of integration is accounted for as ΔP, defined as $\Delta P = P_Z - P_0$ where P_Z is the pressure at the plane of integration and P_0 is the output pressure, 113 Pa (0.85 Torr). In reality, when operating in vacuum, a portion of this pressure thrust will be converted into momentum of the neutrals, this is not accounted for in this treatment.

Using equation 3.5, the thrust produced by a 100 sccm, 450 V, 13.56 MHz discharge with 967 K initial temperature wall is 1.13 mN for a total deposited rf-power of 3.3 W, giving a gross thrust-to-power ratio of 0.34 mN/W. This value compares well to Hall effect (0.05 - 0.08 mN/W)[71,72] and gridded ion (0.01 - 0.02 mN/W)[72] thrusters. Further, The ability to operate the thruster with very low ($\leq$ 5 W) absolute powers provides an advantage over techniques that require a high minimum power to operate, e.g. Arcjets[4,72]. These properties make the Pocket Rocket desirable option for nano sized platforms with little onboard power.

Note that these values represent lab operating conditions where the outlet pressure is set to 113 Pa

(0.85 Torr), as measured in the expansion chamber and the deposited power is taken from the simulation data, see figure 7. If employed in a vacuum the output pressure P_0 will approach zero, resulting in the formation of a sharp pressure drop through the throat of the nozzle[16,73]. Although this boundary will alter the performance of the thruster it will also maintain the pressure gradient through the source and therefore, the heating mechanisms within the source are not expected to change significantly in vacuum.

4 Phase-Resolved Electron-Impact Excitation Rate: Experiments and Simulations

Measured and simulated phase-resolved Ar($2p_1$) excitation rates are shown in Figure 5 (a) and (b), respectively, for an α-mode, 186 Pa (1.4 Torr) plenum pressure, 13.56 MHz, 135 V discharge. The simulated powered electrode potential and dielectric surface potential (Z = 21 mm, R = 2.1 mm) phase aligned with the simulated excitation are shown in figure 5 (c). The experimental data has been shifted in phase such that the excitation structures align with those produced in the simulation.

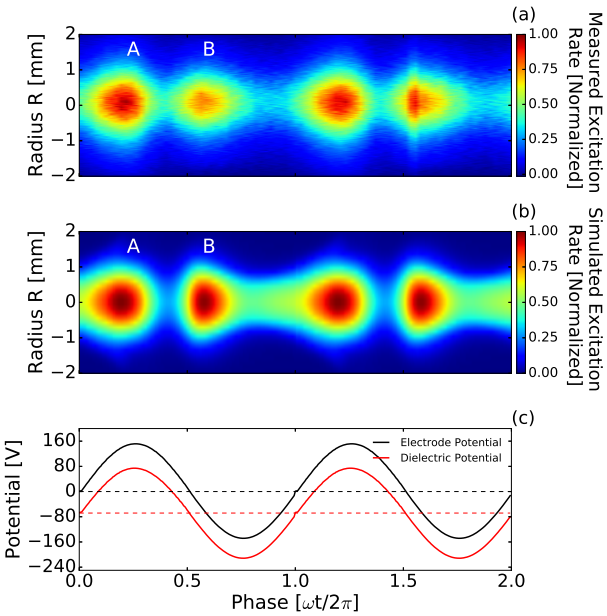

Figure 5: Phase-resolved (a) measured and (b) simulated Ar($2p_1$) excitation rates, and (c) simulated electrode voltage waveform and dielectric surface potential at the powered electrode (Z = 21 mm, R = 2.1 mm) with respect to rf-phase. Plenum pressure 200 Pa (1.5 Torr) in experiment, 186 Pa (1.4 Torr) in simulation, 135 V applied voltage at 13.56 MHz, simulation wall temperature 332 K.

There is close agreement between the experimental measurements and the simulations. Two excitation structures occur per phase cycle in both simulated and measured Ar($2p_1$) excitation rates at 135 V, these have been labelled A and B in figure 5. Peak A is wider temporally than peak B and occurs as the voltage at the powered electrode and adjacent dielectric are increasing, thereby acceler-

ating electrons towards the dielectric, this is the phase of sheath collapse. Peak B occurs for decreasing voltage at the powered electrode and dielectric, accelerating electrons away from the dielectric, this is the phase of sheath expansion.

A similar comparison for a 240 Pa (1.8 Torr) plenum pressure, 13.56 MHz, 445 V discharge is shown in figure 6, where the plasma is operating in a 'bright' mode[74]. This bright mode is hereafter referred to as γ-mode, defined as the point where the integrated excitation from peak C becomes larger than A and B. The discharge transitions into γ-mode for voltages higher than 325 V in experiment and at voltages higher than 270 V in simulation.

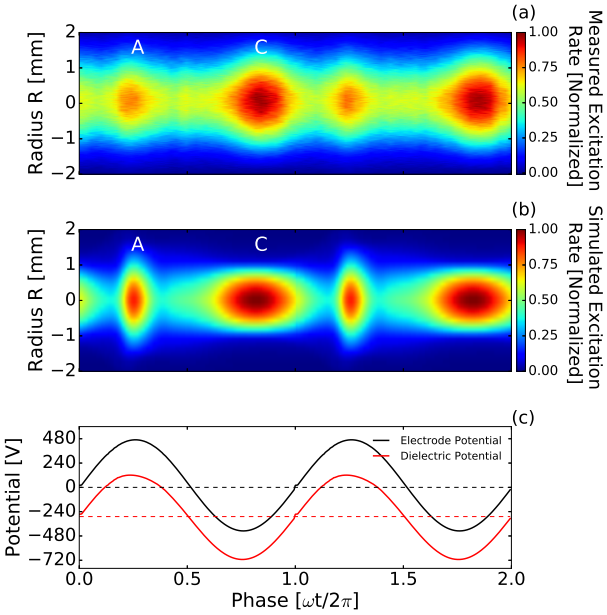

Figure 6: Phase-resolved (a) Measured and (b) simulated Ar($2p_1$) excitation rates, and (c) simulated electrode voltage waveform and dielectric surface potential at the powered electrode (Z = 21 mm,R = 2.1 mm) with respect to rf-phase. Plenum pressure 1.8 Torr in experiment, 1.7 Torr in simulation, 445 V applied voltage at 13.56 MHz, simulation wall temperature 963 K.

The measured and simulated excitation rates show close agreement with two excitation structures per rf-cycle. When compared to figure 5, the excitation during sheath collapse at the powered electrode, peak A, is still visible, however this structure occurs over a shorter time interval. The excitation during sheath expansion at the powered electrode, peak B, is no longer visible and a new excitation structure, peak C, appears just after maximum sheath extension at $\omega t/2\pi \approx 0.75$. Peak C represents excitation from secondary electrons released from the alumina surface via ion bombardment and subsequently accelerated through the sheath potential. Note also that the background excitation rate is higher in γ-mode than in α-mode, suggesting the existence of a time-independent excitation mechanism.

The time-averaged dielectric surface potentials, denoted by the red dotted lines in figures 5 and 6 (c), are both negative. Since the bias on the blocking capacitor is small, the average applied voltage to the electrodes is essentially zero. The charging of the alumina dielectric surface therefore functions as a dc

self-bias voltage, which is most negative for the 445 V case, being negative for 74% of the rf-cycle as compared to 66% cycle at 135 V. In traditional rf discharges, where bare metal electrodes are used and a blocking capacitor is installed in the circuit, the dc self-bias voltage forms to balance the collected currents to the grounded and powered electrodes[30]. In this geometry, the electrodes are not in direct contact with the plasma, and so currents to those electrodes are displacement currents. Assuming the current density is constant, the dc self-bias voltage is determined by the ratio of the collecting areas of the grounded and powered electrodes. For those conditions the dc self-bias voltage scales linearly with the applied voltage amplitude, and is negative if the powered electrode has a smaller surface area, as in this geometry.

The computed increase in the magnitude of the dc self-bias voltage with increasing applied voltage is a result of several factors. First, an increase in the driving voltage naturally produces an increase in the dc self-bias voltage, for all other conditions remaining constant. Second, with increasing applied voltage and power deposition, the plasma density increases, which reduces the sheath width near the powered electrode relative to that adjacent to the grounded electrodes. This leads to an increase in capacitance, which enables more current to be collected by the powered electrode, thereby making the negative dc self-bias voltage a larger fraction of the applied voltage[30,75]. Third, an increase in the ion flux due to the increased density releases more secondary electrons at the radial alumina wall adjacent to the powered electrode. These secondary electrons are accelerated to higher energies through the sheath potential as the dielectric surface potential is more negative. As the dc self-bias voltage varies along the axial length of the thruster, so too does the flux and energy of ion-induced secondary electrons, which could potentially lead to an additional secondary electron induced asymmetry[76].

4.1 Power Dissipated in the Plasma

The measured and simulated plasma power deposited with respect to applied voltage is shown in figure 7:

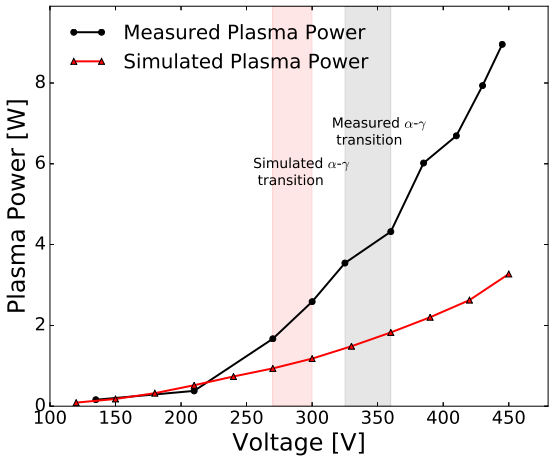

Figure 7: Measured and simulated plasma power with respect to applied voltage amplitude. The voltage interval within which the α-γ transition occurs is shown by shaded regions. Plenum pressure 200 - 240 Pa (1.5 - 1.8 Torr) in experiment, 186 - 226 Pa (1.4 - 1.7 Torr) in simulation, for 13.56 MHz driving voltage, simulation wall temperature 332 - 963 K.

The measured plasma power agrees with the simulated power for voltages up to approximately 250 V, beyond which the measured plasma power increases more rapidly with voltage. An α-γ mode transition occurs for applied voltages between 325 V and 355 V in the experiment and between 270 V and 300 V in simulation. This difference in the α-γ mode transition voltage could be due to ion-energy dependent secondary electron emission coefficients that are not captured in the model. These differences could also be due to power deposition in non-plasma components within the circuit, which are not accounted for in the model.

The more gradual increase in power deposition with voltages above 250 V in simulation is attributed to: (1) the secondary electron emission and thermal accommodation coefficients will affect the power deposition to the plasma. These values are not precisely known in the experiment, and can change depending on material temperature and surface cleanliness[77,78], (2) by increasing the initial wall temperature with the applied voltage using the two step method, the conductive losses from the neutral gas to the walls are reduced for a fixed thermal accommodation coefficient. Less power is required to attain higher neutral gas temperatures as the power required to maintain the high wall temperature is effectively removed from the simulation. This results in a lower simulated plasma power deposition for the given applied voltage.

5 Spatio-Temporal Heating Mechanisms in the Pocket Rocket

5.1 Phase-averaged Plasma Parameters

The Ar^+ density, electron temperature, axial pressure profile and axial neutral velocity profile are shown in figures 8 (a), (b) and (c), respectively, for a 450 V, 1.7 Torr plenum pressure γ-mode

discharge.

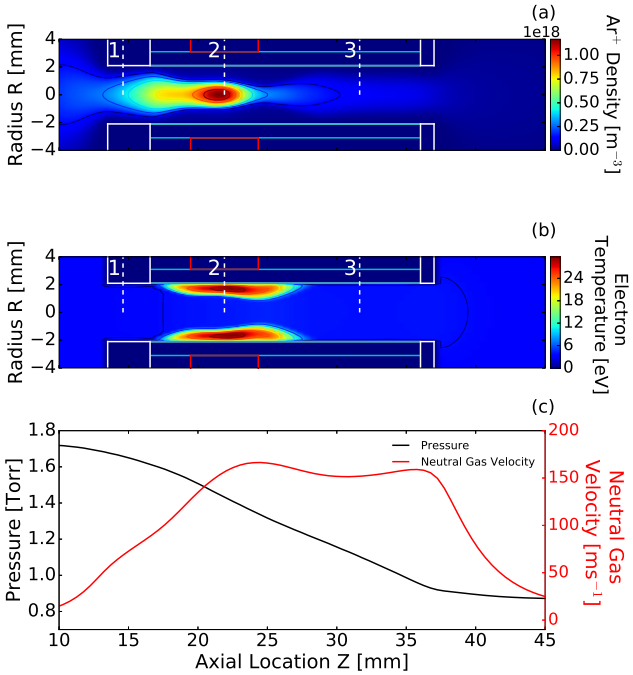

Figure 8: Phase-averaged (a) Ar^+ density (b) electron temperature and (c) on-axis gas pressure and axial neutral gas velocity. Regions 1, 2 and 3 are defined as upstream, powered electrode and downstream, respectively. Plenum pressure 226 Pa (1.7 Torr) in argon, 450 V applied voltage at 13.56 MHz, wall temperature 967 K. An axial location of zero is at the top of the plenum.

The Ar^+ density, figure 8 (a), reaches a maximum on-axis at the centre of the powered electrode (region 2). The decrease in density from upstream to downstream (regions 1 to 3) is primarily a result of the decreasing pressure. The inhomogeneous axial plasma density results in an axial variation in sheath thickness and capacitance, leading to larger variations in current collected at the powered and grounded electrodes.

There is an asymmetry in electron temperature about the powered electrode in figure 8 (b), with a region of hotter electrons reaching closer to the axis further downstream (region 3). The phase-averaged sheath extension can be inferred from the region of hot electrons, as cold electrons will not have enough energy to enter this region. This suggests a larger sheath extension downstream (region 3) of the powered electrode relative to upstream (region 1). This is in agreement with the asymmetric distribution of plasma density observed in figure 8 (a). The electron temperatures upstream and downstream of the source (regions 1 and 3, respectively) are significantly lower than at the powered electrode (region 2).

The on-axis neutral gas pressure (P_g) and axial neutral gas velocity (V_g) are shown in figure 8 (c). The pressure decreases linearly with respect to distance until it reaches ≈ 0.85 Torr, equal to the output pressure in the expansion region. The neutral gas velocity increases as it enters the thruster (region 1), reaching a maximum at the powered electrode (region 2) where power is primarily deposited

into the plasma. The gas velocity drops sharply as it expands and cools upon exiting the thruster at Z = 37 mm (region 3), where $V_g \propto \sqrt{T_g}$ as expected.

The total simulated phase averaged Ar($2p_1$) excitation rate due to collisions with fluid electrons, created in the gas-phase, and secondary, Monte-Carlo, electrons is shown in figure 9 (a). The on-axis contributions from each class of electrons to the total excitation rate are shown in figure 9 (b) and the on-axis plasma potential and dielectric surface potential, (R,Z = 2.1 mm, 21 mm), are shown in 9 (c).

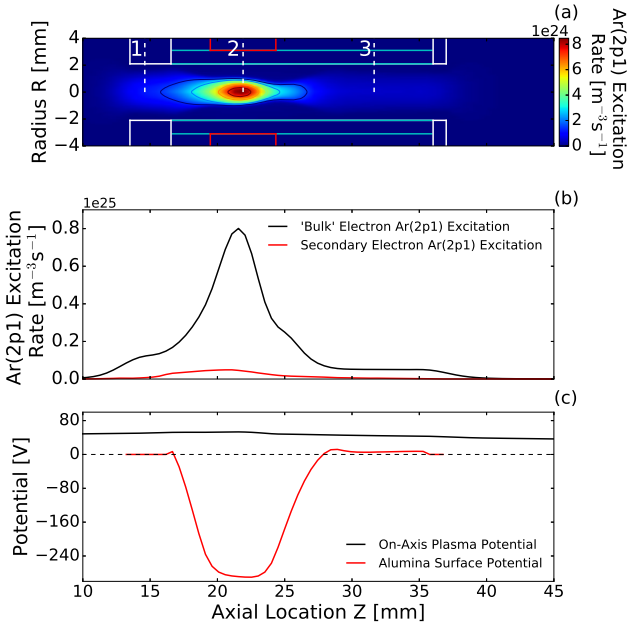

Figure 9: Phase-averaged (a) Ar($2p_1$) total excitation rate, (b) on-axis contribution to the excitation rate from fluid electrons and secondary electrons, and (c) on-axis plasma potential and dielectric surface potential at the powered electrode (region 2). Plenum pressure 226 Pa (1.7 Torr) argon, 450 V applied voltage at 13.56 MHz, wall temperature 967 K. An axial location of zero is at the top of the plenum.

There is a peak in Ar($2p_1$) excitation rate at the powered electrode (region 2), aligned with the region of negative dc self-bias voltage on the alumina surface as shown in figure 9 (c). The excitation rate upstream and downstream (regions 2 and 3, respectively) is significantly lower than at the powered electrode as is consistent with a γ-mode discharge.

The on-axis Ar($2p_1$) excitation rate resulting from collisions with either fluid or secondary electrons is shown in figure 9 (b). Although upstream (region 1) has a higher peak excitation than downstream (region 3), their axially integrated contributions are approximately the same, noting that the volume of excitation upstream is larger than downstream. The excitation is primarily driven by lower energy fluid electrons in all three regions, as the more energetic secondary electrons preferentially cause ionization. The secondary electron ionization rate (not shown) is a factor of 5 larger than the excitation rate and is approximately equal to the ionization rate of the fluid electrons in γ-mode.

The excitation peaks upstream and downstream (regions 1 and 3) have almost no contribution from secondary electrons. Excitation in these regions arises primarily from sheath heating mechanisms,

where time varying electric fields ensure current continuity between the central powered electrode and the grounded electrodes at the inlet and outlet. The physical mechanisms responsible for the excitation at each location are discussed in sections 5.2 and 5.4.

The contribution to the total excitation rate by secondary electrons is greatest at the powered electrode (region 2). This is to be expected as the dc self-bias voltage at the surface of the dielectric wall, shown in figure 9 (c), is most negative at the powered electrode between $17 \leq Z \leq 27$ mm. The magnitude of the dc self-bias voltage in region 2 and corresponding axial positive ion flux at regions 1, 2 and 3 with respect to applied voltage are shown in figures 10 (a) and (b), respectively. The small statistical scatter is due to the inherent noise in the Monte Carlo simulation used to track secondary electrons.

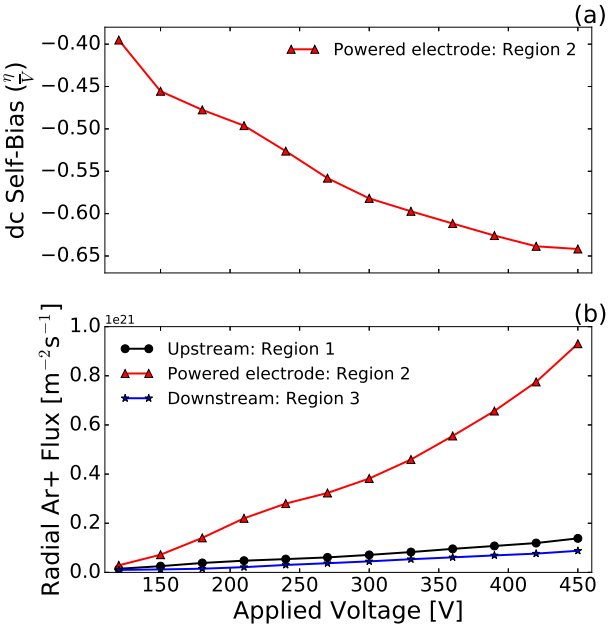

Figure 10: Phase-averaged (a) dc self-bias voltage and (b) Ar+ flux at the alumina surface with respect to applied voltage amplitude upstream (region 1), at the powered electrode (region 2) and downstream (region 3). Plenum pressure 186 - 226 Pa (1.4 - 1.7 Torr) argon, 13.56 MHz applied voltage, alumina wall temperature 334 - 967 K.

Normalizing the dc self-bias voltage to the applied voltage more clearly shows the increasing ratio with increasing applied voltage. The dc self-bias voltage approaches a limit of 65% - 70% of the applied voltage amplitude. This corresponds to a dc self-bias voltage of -304 V for 450 V applied at the powered electrode. Due to the large physical asymmetry between the powered and grounded electrode areas, the dc self-bias voltage is a large fraction ($\geq$ 40%) of the applied voltage amplitude even when the discharge is operating in α-mode.

Increasing the applied voltage results in an increased phase-averaged ion flux at all axial locations as shown in figure 10 (b). The increase is greatest in magnitude at the powered electrode (region 2), correlating with the increased dc self-bias voltage and production of more secondary electrons.

The secondary electrons produced at the powered electrode (region 2) are also accelerated to higher energies than those produced at the grounded electrodes. The increased ionization due to ion-induced secondary electron emission results in an increase in the plasma density at the powered electrode (region 2) as shown in figure 11:

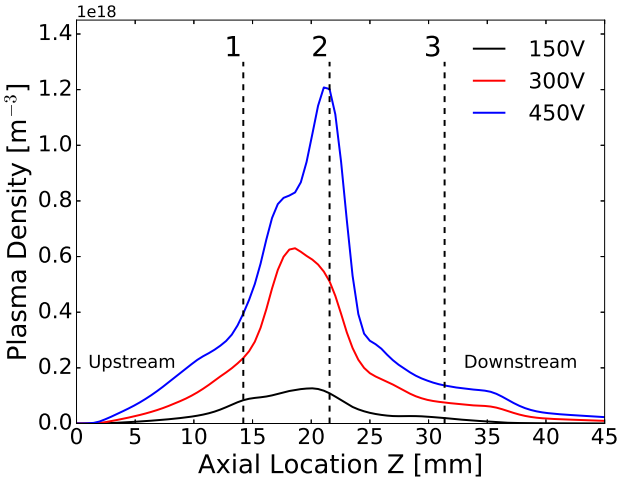

Figure 11: Phase-averaged on-axis plasma density with respect to axial location for 150 V, 300 V, and 450 V discharges. The discharge is in α-mode at 150 V and γ-mode for 300 V and 450 V. Plenum pressure 186 Pa, 213 Pa, 226 Pa, (1.4 Torr, 1.6 Torr, 1.7 Torr) argon, 13.56 MHz applied voltage, wall temperature 334 K, 687 K, 963 K, respectively. An axial location of zero is at the top of the plenum.

In α-mode, 150 V, the plasma density reaches a maximum of 1.1×10^{17} m^{-3} near the centre of the powered electrode (region 2). A secondary peak in plasma density occurs upstream (region 1). The plasma density drops off sharply at Z $\geq$ 37 mm as the plasma expands at the exit of the thruster. As the voltage is increased to 300 V, the plasma enters γ-mode and the maximum on-axis plasma density increases to 6×10^{17} m^{-3} at the upstream side of the powered electrode (Z = 17 mm, between regions 1 and 2). This value closely agrees with a value of 5.4×10^{17} m^{-3} previously obtained for similar operating conditions at 300 V[16].

At voltages above 300 V the peak density shifts back to the centre of the powered electrode (region 2) at Z = 21 mm reaching a maximum value of 1.2×10^{18} m^{-3} at 450 V. The increase in density at this location is attributed to the production of more energetic secondary electrons as the dc-self bias voltage magnitude and ion flux increase. The smaller peak at approximately Z = 17 mm results from electron heating during sheath collapse upstream of the powered electrode (region 1). The spatial distribution of these heating mechanisms is described in more detail in section 5.4.

The neutral gas temperature and rf power deposition for a simulated 1.7 Torr argon, 450 V (γ-mode), 13.56 MHz discharge are shown in figure 12.

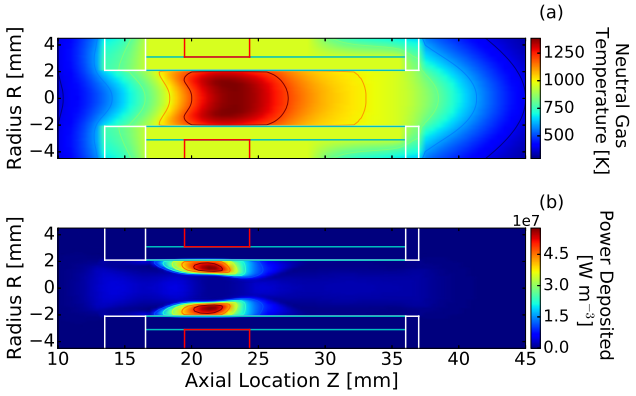

Figure 12: Phase-averaged (a) neutral gas temperature, and (b) rf power deposition for a 450 V, γ-mode discharge. Plenum pressure of 226 Pa (1.7 Torr), 13.56 MHz applied voltage with 963 K wall temperature. An axial location of zero is at the top of the plenum.

The largest increase in neutral gas temperature is axially localized near the powered electrode (region 2), shown in 12 (a). This correlates with the region of highest dc self-bias voltage (figure 9 (c)), greatest radial Ar^+ flux (figure 10 (b)) and greatest plasma density (figure 11). The ions first gain thermal energy in the presheath and then radial advective velocity in the sheath, both of which contribute to gas heating via charge exchange collisions. This is in agreement with previous observations, which have suggested that the primary neutral gas heating mechanism is through ion-neutral charge exchange collisions[17,21]. Localized heating close to the powered electrode reduces the local gas density, resulting in a reduction in collisionality as shown previously in figure 4.

The rf power coupled to the plasma per unit volume is shown in figure 12 (b). The total rf power coupled to the plasma is 3.27 W, of this 2.69 W is coupled via ion acceleration in the sheaths, and 0.58 W is coupled via electron heating. Power deposition is highest adjacent to the powered electrode between $17 \leq Z \leq 27$ mm, aligning with the region of highest dc self-bias voltage. Power is primarily deposited within the sheaths and reduces with radial distance from the radial wall, dropping significantly for $R \leq 1.0$ mm. The net rate of charge exchange is largest in the center of the bulk plasma where the ion density is highest. However, the heat source is largest off axis, in the sheaths, where the ions gain energy. It follows that a larger sheath region will result in a larger number of ions being accelerated over a greater distance, and will increase the volume of the plasma into which power is coupled. Furthermore a larger maximum sheath extension necessitates an increase in the sheath velocity, for a fixed driving frequency, increasing the power deposition.

Since the maximum sheath extension is proportional to the radial wall surface potential, an increasingly negative dc self-bias voltage increases the sheath extension and consequentially the volume

of plasma into which power is deposited[30,75]. The sheath extension is also inversely proportional to the decreasing gas density, resulting in an increased radial extent to which power is deposited with increasing axial distance along the thruster. Combining these two effects, the volume of the plasma into which power is deposited could be optimized for a given radius by varying the dc self-bias voltage. This could be accomplished by varying the size of the grounded electrode relative to the powered electrode, a technique used in semiconductor processing[37,79], or through an application of an electrical asymmetry[20,80].

The high radial ion acceleration and ion flux close to the powered electrode results in an undesired etching of the dielectric surface. Figures 13 (a) and (b) show the angular distribution in the ion energy distribution function (IEDF) and angle integrated IEDF incident on the alumina wall adjacent to the powered electrode (R,Z = 2.1 mm,21 mm) for a 450 V γ-mode discharge:

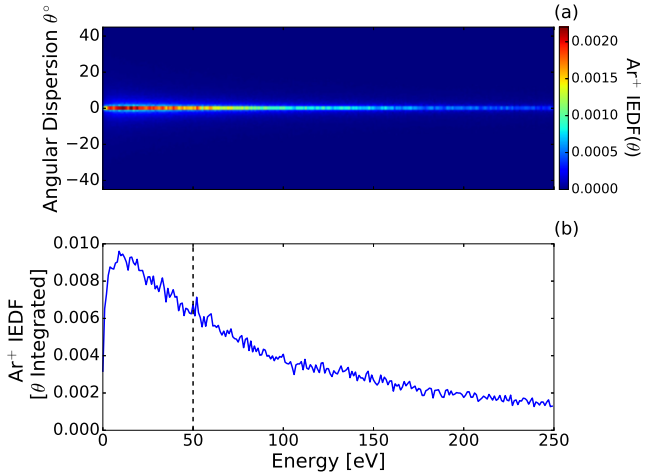

Figure 13: Phase-averaged (a) angularly resolved and (b) angle integrated Ar^+ ion energy distribution function adjacent to the powered electrode dielectric at region 2 (R,Z = 2.1 mm,21 mm) for a 450 V γ-mode discharge. Plenum pressure 226 Pa, (1.7 Torr) argon, 13.56 MHz at 450 V, wall temperature 963 K

Figure 13 (a) shows the angular dispersion of the ions impacting the dielectric surface with respect to the ion energy, the colour denoting the fraction of the IEDF at the given energy. Over 50% of ions impacting the radial wall hit within 2° of normal, accelerated through the powered electrode sheath. This indicates that the radial ion acceleration is substantial enough such that the radial ion flux is not greatly affected by the perpendicular neutral flow.

The IEDF in figure 13 (b) is Maxwellian in profile due to the high gas pressure, and has a mode energy of 10 eV. There exists a high energy tail extending beyond 250 eV due to the relatively large potential (-342 V) present across the powered electrode sheath. The high energy tail contains the majority of the ion population, with 61% of the ions above 50 eV, denoted by the dashed line. This indicates that sputtering of the alumina surface is likely to occur during γ-mode operation.

As sputtering rates scale linearly with the ion current density incident on the surface to be sput-

tered[75], an estimate of the etching rate in the Pocket Rocket can be achieved by comparison to known devices. Alumina etching rates of 10 nm/min have been demonstrated using an industrial ion milling technique employing a 500 eV, 1 mA cm^{-2} current density Ar^+ beam[81]. The Ar^+ radial flux incident on the wall at 450 V in the Pocket Rocket is 9.3×10^{20} [m^{-2}s^{-1}], see figure 10 (b), which equals a current density of 14.9 mA cm^{-2}. By comparison to Ref. 81 the etching rate in the Pocket Rocket is therefore approximately 149 nm/min. This reduces to an effective etching rate of 90.9 nm/min, 5.45 μm/hour, assuming that only 61% of the ions are capable of sputtering. However, as this does not fully account for the reduced mean ion energy or the increased surface redeposition due to the higher operating pressure in the Pocket Rocket, these values represent an upper limit for the etching rate.

Etching rates decrease by approximately a factor of three per order of magnitude in ion energy, this is due to the dependence of the sputtering yield on the ion velocity[82]. If this, along with a conservative redeposition fraction of 0.5, is assumed then the final net etching rate in the Pocket Rocket becomes 0.91 μm/hour. At this rate the Pocket Rocket could operate for over 1000 hours before the alumina wall was significantly etched, the lifetime of the thruster is therefore expected to be constrained primarily by propellant availability and not through component etching.

5.2 Phase-Resolved Electron Heating Mechanisms

The predicted phase-resolved total Ar($2p_1$) excitation rate on-axis and alumina surface bias for three operating voltages (150 V, 300 V, 450 V) are shown in figures 14 (a) and (b), respectively. The excitation profiles are integrated through a depth of field equal to the length of the source (DoF = 24 mm), including excitation from each region of interest.

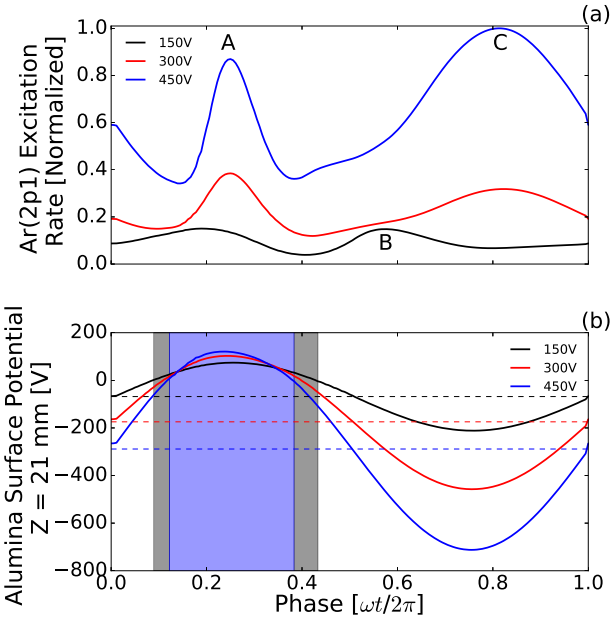

Figure 14: Simulated (a) on-axis phase-resolved Ar($2p_1$) excitation and (b) dielectric surface potential at the powered electrode (region 2), (R, Z) = (2.1 mm, 21 mm), for applied voltages 150 V, 300 V, 450 V. The shaded area represents the phase interval for which the sheath is collapsed for operation at 150 V (black) and 450 V (blue). Plenum pressure 186 Pa, 213 Pa, 226 Pa, (1.4 Torr, 1.6 Torr, 1.7 Torr) argon, 13.56 MHz, wall temperature 334 K, 687 K, 963 K, respectively.

Peak A occurs for all three voltages in figure 14 (a) and increases in magnitude with applied voltage. The peak becomes more temporally narrow and more closely aligned with the maximum voltage at the powered electrode (region 2) dielectric surface as the applied voltage is increased. This change is a result of the differing charge dynamics of the ions and electrons within a phase cycle leading to the build up of excess charge within the plasma bulk. Increasing the applied voltage results in a larger dc self-bias voltage and a greater phase-averaged radial ion flux as shown previously in figure 10. To maintain quasi-neutrality within the bulk there is an equal phase-averaged electron flux to the walls to compensate the positive ion loss from the plasma[83]. During sheath collapse, shown in figure 14 (b) as the shaded regions, electrons are able to leave the bulk plasma to conserve current continuity. However, as the dc self-bias voltage increases the phase-averaged positive Ar^+ flux leaving the plasma increases, indicated in figure 10 (b) as an increased phase-averaged positive ion flux. The electron flux at the phase of sheath collapse must therefore increase with increasing voltage. Further, the proportion of the rf-phase cycle for which the sheath is collapsed decreases with increasing dc self-bias voltage, observed as a reduction in the shaded area between 150 V and 450 V operation in figure 14 (b). Both of these mechanisms lead to increased electron flux at sheath collapse and therefore a higher Ar($2p_1$) excitation rate.

Peak B occurs for voltages below 150 V and is approximately the same magnitude as peak A. Peak B is produced as the alumina surface potential decreases, repelling electrons from the surface, and can

therefore reasonably be attributed to sheath expansion heating. Due to the high pressures ($\geq$ 1 Torr), the maximum sheath velocity is relatively low and this results in a relatively small contribution to the total excitation.

Peak C occurs just after the phase of most negative alumina surface potential ($\frac{\omega t}{2\pi} = 0.77$), indicating that it is not a product of sheath movement. The excitation could be due to the release of energetic secondary electrons from the alumina surface, which are then accelerated through the fully extended sheath. Electrons produced at material surfaces have a non-zero time of flight to reach the central axis of the Pocket Rocket and hence there will be a delay between maximum ion bombardment, at most negative voltage, and when the on-axis excitation occurs due to secondary electrons. Note also that the shape of the surface potential in figure 14 is sinusoidal, indicating that the rf voltage waveform is not greatly deformed as it is coupled between the copper electrode through the alumina radial wall. This is due, in part, to the current to the electrodes through the alumina being purely displacement current, and the permittivity of the alumina in the model being independent of temperature and electric field strength.

5.3 Phase resolved excitation across the α-γ mode transition

An α-γ mode transition is observed experimentally as an increase in the optical emission intensity at voltages above 325 V and in simulation as an increase in the Ar($2p_1$) excitation at voltages above 270 V. The simulated on-axis Ar($2p_1$) excitation rates for voltages between 120 - 450 V, in steps of 30 V, are shown with respect to phase in figure 15, where the contours are obtained by interpolating the excitation between each voltage.

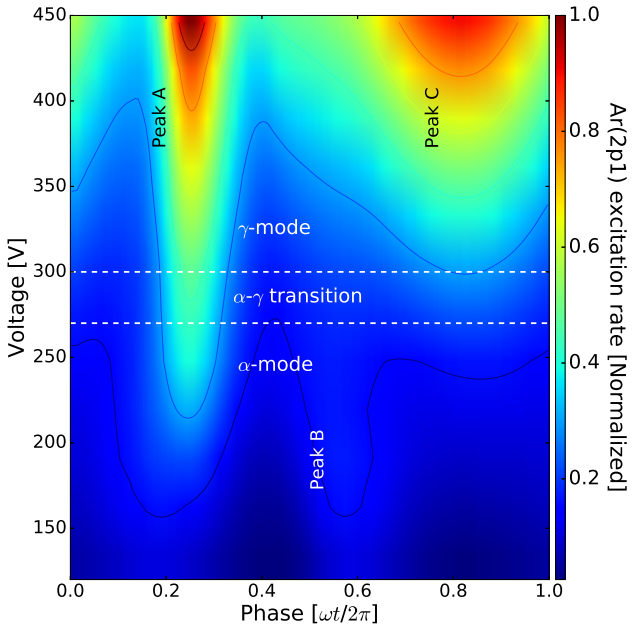

Figure 15: Simulated Ar($2p_1$) excitation rates, including excitation from fluid and secondary electrons, with respect to rf voltage phase and voltage amplitude. Voltages below 270 V and above 300 V (inclusive) denote for α-mode and γ-mode operation, respectively. Plenum pressure 186 - 226 Pa (1.4 - 1.7 Torr), 13.56 MHz, wall temperature 334 - 963 K.

Peaks A and C grow with increasing applied voltage, as shown previously in figure 14, while peak B either reduces with increasing voltage or does not grow fast enough to overcome the increasing time-independent 'background' excitation between peaks A and C. This background excitation is also observed experimentally as shown in figure 6 (a). The increase the temporally constant background excitation is attributed to the secondary electron emission as a result of increased temporally constant ion bombardment, shown in figure 10 (b). This implies that there is time-independent neutral gas heating as ion-neutral charge exchange is the primary neutral energy deposition pathway[21]. Although the dc self-bias voltage ensures an approximately time-independent secondary electron rate of production, the secondary electron energy has a time dependency. The most energetic secondary electrons are produced at maximum sheath extension aligning with excitation peak C. Therefore, the background emission is an indication of the temporally constant secondary electron production, whereas peak C describes the temporally varying secondary electron energy.

As described previously, Peak A primarily results from increased axial and radial electron flux during sheath collapse at the powered electrode to maintain current continuity and Peak B results from electron collisions during sheath expansion. Peak C and the background excitation result from secondary electrons generated from ion bombardment. As described in section 4, an α-γ mode transition occurs when the secondary electron interactions represent the dominant ionization pathway, i.e. time-integrated excitation from Peak C and the background is greater than the combined excitation from peak A and B. This transition occurs in simulation between 270 V and 300 V, denoted between

the white dotted lines in figure 15, closely matching the experimental transition at 325 V.

5.4 Spatially resolved plasma heating mechanisms

Simulated, phase-resolved, on-axis Ar($2p_1$) excitation rates from upstream, at the powered electrode and downstream of the source, regions 1, 2 and 3, respectively are shown in figure 16. By setting the DoF to 0.5 mm, one cell thick in the axial direction, the excitation rate at each location can be observed independently as opposed to the axially integrated analysis discussed earlier. The phase-resolved excitation from each region for a 226 Pa (1.7 Torr) plenum pressure, 13.56 MHz, 450 V, γ-mode discharge is shown in figure 16 (a) and the voltage drop across the sheath ($V_{on-axis}$ - $V_{dielectric}$) at each region in figure 16 (b). Note that the phase of maximum sheath drop at the grounded electrodes is $\frac{\omega t}{2\pi} = 0.5$ out of phase relative to the maximum sheath drop at the powered electrode.

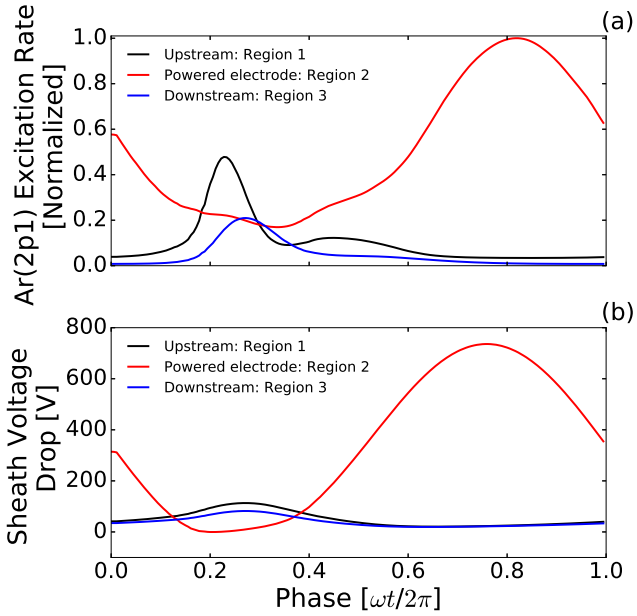

Figure 16: Simulated on-axis (a) Ar($2p_1$) excitation and (b) sheath voltage drop upstream, at the powered electrode and downstream, regions 1, 2 and 3, respectively. Plenum pressure 226 Pa (1.7 Torr), 450 V applied voltage at 13.56 MHz, wall temperature 963 K.

The phase-resolved Ar($2p_1$) excitation is normalized to the global maximum value within the three profiles shown in figure 16 (a). A significant change in the temporal excitation profile between the three regions demonstrates that the dominant excitation mechanism changes with axial distance. The excitation upstream (region 1) peaks just prior to the maximum sheath drop, and hence maximum sheath extension, at the upstream grounded electrode. This indicates that sheath expansion heating is the dominant electron heating mechanism at the upstream grounded electrode[34]. A secondary, smaller, peak in excitation during sheath collapse ($0.3 \leq \frac{\omega t}{2\pi} \leq 0.5$) suggests sheath collapse heating occurs in this region as well.

Excitation at the downstream grounded electrode (region 3) exhibits a similar profile as the upstream, albeit shifted to a later time in the rf cycle and shows no excitation during sheath collapse. Although the maximum sheath voltage drop across the downstream grounded electrode sheath is lower than that for the upstream, it occurs over the same region in rf phase ($0.1 \leq \frac{\omega t}{2\pi} \leq 0.5$) shown in figure 16 (b). This suggests that the primary heating mechanism is likely still sheath expansion heating at the grounded electrode, however there may be further effects from other heating mechanisms such as axial electron flux towards the collapsed powered electrode sheath. Upstream and downstream (regions 1 and 3, respectively) both demonstrate heating mechanisms that correspond to α-mode heating, where sheath expansion and collapse dictate the ionization and excitation structures.

The excitation at the powered electrode (region 2), is markedly different from that upstream and downstream (regions 1 and 3, respectively). Most notably, the peak excitation rate occurs later in the rf cycle, just after the phase of maximum sheath voltage drop $\frac{\omega t}{2\pi} = 0.8$. This corresponds to the phase of most negative alumina surface potential, suggesting that the excitation is most likely due to collisions from an increased number of high energy secondary electrons, accelerated through the sheath potential as previously described with reference to figure 14. The excitation structure at the powered electrode (region 2) shows little evidence of either sheath expansion or sheath collapse heating during the powered electrode sheath collapse, $\frac{\omega t}{2\pi} \approx 0.25$, but does show a substantial 'background' excitation, such that the minimum excitation rate at the powered electrode is only slightly less than the maximum rate downstream (region 3). This background excitation increases with voltage due to the ion-induced secondary electron emission increasing with the phase-averaged ion flux, providing a time-independent excitation mechanism as shown in figure 6.

6 Conclusions

Electron heating mechanisms have been investigated in a radio-frequency (rf) electrothermal microthruster operating between 186 - 226 Pa (1.4 - 1.7 Torr) with an applied 13.56 MHz voltage between 130 - 450 V. Experimental measurements of the phase-resolved Ar($2p_1$) excitation rate have been compared to simulations using the Hybrid Plasma Equipment Model, showing close agreement. An α-γ mode transition was observed for voltages above 270 V in simulation and above 325 V in the experiment. Three excitation structures were observed within the rf voltage cycle, and by comparison to simulations, the primary heating mechanism responsible for each was identified: electron heating at the collapsing sheath edge during sheath collapse, electron heating during sheath expansion and secondary electron induced excitation at maximum sheath extension. Sheath collapse and sheath expansion heating mechanisms primarily deposit power on-axis at the upstream and downstream ends

of the thruster, while power deposition from secondary electron collisions and ion-neutral charge exchange interactions predominately occurs within the powered electrode sheath. The maximum sheath extension, and correspondingly the heated volume of the plasma, was found to increase with the magnitude of the dc self-bias voltage. Optimising the volume of propellant heated, and the plasma discharge mode, via the dc self-bias voltage could potentially enable the development of more power efficient electrothermal thrusters for use on increasingly miniaturized satellite platforms.

7 Acknowledgements

The authors wish to thank P. Hill, R. Armitage, C. Murphy and E. Wagenaars for their technical support and useful discussions. The work presented herein was funded by the Engineering and Physical Sciences Research Council (EPSRC), grant reference number: EP/m508196/1. The participation of M. Kushner was supported by the US National Science Foundation and the US Department of Energy Office of Fusion Energy Science.

8 References

[1] I. Levchenko, K. Bazaka, Y. Ding, Y. Raitses, S. Mazouffre, T. Henning, Peter J. Klar, S. Shinohara, J. Schein, L. Garrigues, M. Kim, D. Lev, F. Taccogna, R. W. Boswell, C. Charles, H. Koizumi, Y. Shen, C. Scharlemann, M. Keidar, and S. Xu. Space micropropulsion systems for Cubesats and small satellites: From proximate targets to furthermost frontiers. 5(1), 2018. ISSN 19319401. doi:10.1063/1.5007734.

[2] I. Adamovich, S. D. Baalrud, A. Bogaerts, P. J. Bruggeman, M. Cappelli, V. Colombo, U. Czarnetzki, U. Ebert, J. G. Eden, P. Favia, D. B. Graves, S. Hamaguchi, G. Hieftje, M. Hori, I. D. Kaganovich, U. Kortshagen, M. J. Kushner, N. J. Mason, S. Mazouffre, S. Mededovic Thagard, H. R. Metelmann, A. Mizuno, E. Moreau, A. B. Murphy, B. A. Niemira, G. S. Oehrlein, Z. Lj Petrovic, L. C. Pitchford, Y. K. Pu, S. Rauf, O. Sakai, S. Samukawa, S. Starikovskaia, J. Tennyson, K. Terashima, M. M. Turner, M. C.M. Van De Sanden, and A. Vardelle. The 2017 Plasma Roadmap: Low temperature plasma science and technology. *Journal of Physics D: Applied Physics*, 50(32), 2017. ISSN 13616463. doi:10.1088/1361-6463/aa76f5.

[3] D. B. Scharfe and A. D. Ketsdever. A Review of High Thrust , High Delta-V Options for Microsatellite Missions. *45th AIAA/ASME/SAE/ASEE Joint Propulsion Conference*, 15(August):1–14, 2009.

[4] M. Martinez-Sanchez and J. E. Pollard. Spacecraft Electric Propulsion-An Overview. *Journal of Propulsion and Power*, 14(5):688–699, 1998. ISSN 0748-4658. doi:10.2514/2.5331.

[5] Y. Ulybyshev. Satellite Constellation Design for Complex Coverage. *Journal of Spacecraft and Rockets*, 45(4): 843–849, 2008. doi:10.2514/1.35369.

[6] M. Keidar, T. Zhuang, A. Shashurin, G. Teel, D. Chiu, J. Lukas, S. Haque, and L. Brieda. Electric propulsion for small satellites. *Plasma Physics and Controlled Fusion*, 57(1), 2015. ISSN 13616587. doi:10.1088/0741-3335/57/1/014005.

[7] A. Poghosyan and A. Golkar. CubeSat evolution: Analyzing CubeSat capabilities for conducting science missions. *Progress in Aerospace Sciences*, 88(November 2016):59–83, 2017. ISSN 03760421. doi:10.1016/j.paerosci.2016.11.002.

[8] D. Rafalskyi and A. Aanesland. Brief review on plasma propulsion with neutralizer-free systems. *Plasma Sources Science and Technology*, 25(4), 2016. ISSN 13616595. doi:10.1088/0963-0252/25/4/043001.

[9] C. Charles, R. W. Boswell, and K Takahashi. Investigation of radiofrequency plasma sources for space travel. *Plasma Physics and Controlled Fusion*, 54(12):124021, 2012. ISSN 0741-3335. doi:10.1088/0741-3335/54/12/124021.

[10] C. Charles. Plasmas for spacecraft propulsion. *Journal of Physics D: Applied Physics*, 42(16):163001, 2009. ISSN 0022-3727. doi:10.1088/0022-3727/42/16/163001.

[11] A. Dunaevsky, Y. Raitses, and N. J. Fisch. Plasma acceleration from radio-frequency discharge in dielectric capillary. *Applied Physics Letters*, 88(25):10–13, 2006. ISSN 00036951. doi:10.1063/1.2214127.

[12] D. M. Goebel and I. Katz. *Fundamentals of Electric Propulsion*. Hokoken, NJ: Wiley, 2008.

[13] C. Charles and R. W. Boswell. Measurement and modelling of a radiofrequency micro-thruster. *Plasma Sources Science and Technology*, 21(2):022002, 2012. ISSN 0963-0252. doi:10.1088/0963-0252/21/2/022002.

[14] C. Charles, J. Dedrick, R. W. Boswell, D. O'Connell, and T. Gans. Nanosecond optical imaging spectroscopy of an electrothermal radiofrequency plasma thruster plume. *Applied Physics Letters*, 103(12):124103, 2013. ISSN 00036951. doi:10.1063/1.4821738.

[15] A. Greig, C. Charles, and R. W. Boswell. Simulation of main plasma parameters of a cylindrical asymmetric capacitively coupled plasma micro-thruster using computational fluid dynamics. *Frontiers in Physics*, 2(January): 1–9, 2015. ISSN 2296-424X. doi:10.3389/fphy.2014.00080.

[16] T. S. Ho, C. Charles, and R. W. Boswell. A Comprehensive Cold Gas Performance Study of the Pocket Rocket Radiofrequency Electrothermal Microthruster. *Frontiers in Physics*, 4(January):1–16, 2017. ISSN 2296-424X. doi:10.3389/fphy.2016.00055.

[17] T. S. Ho, C. Charles, and R. Boswell. Neutral gas heating and ion transport in a constricted plasma flow. *Physics of Plasmas*, 24(8):8–13, 2017. ISSN 10897674. doi:10.1063/1.4996014.

[18] A. Greig, C. Charles, R. Hawkins, and R. Boswell. Direct measurement of neutral gas heating in a radio-frequency electrothermal plasma micro-thruster. *Applied Physics Letters*, 103(7):1–7, 2013. ISSN 00036951. doi:10.1063/1.4818657.

[19] C. Charles, W. Liang, L. Raymond, J. Rivas-Davila, and R. W. Boswell. Vacuum Testing of a Miniaturized Switch Mode Amplifier Powering an Electrothermal Plasma Micro-Thruster. *Frontiers in Physics*, 5(August):1–8, 2017. ISSN 2296-424X. doi:10.3389/fphy.2017.00036.

[20] B. G. Heil, U. Czarnetzki, R. P. Brinkmann, and T. Mussenbrock. On the possibility of making a geometrically symmetric RF-CCP discharge electrically asymmetric. *Journal of Physics D: Applied Physics*, 41(16):165202, 2008. ISSN 0022-3727. doi:10.1088/0022-3727/41/16/165202.

[21] A. Greig, C. Charles, N. Paulin, and R. W. Boswell. Volume and surface propellant heating in an electrothermal radio-frequency plasma micro-thruster. *Applied Physics Letters*, 105(5):054102, 2014. ISSN 0003-6951. doi:10.1063/1.4892656.

[22] H. D. Hagstrum. Theory of auger ejection of electrons from metals by ions. *Physical Review*, 96(2):336–365, 1954. ISSN 0031899X. doi:10.1103/PhysRev.96.336.

[23] T. Lafleur and J.-P. Booth. Control of the ion flux and ion energy in CCP discharges using non-sinusoidal voltage waveforms. *Journal of Physics D: Applied Physics*, 45(39):395203, 2012. ISSN 0022-3727. doi:10.1088/0022-3727/45/39/395203.

[24] C. Charles, R. Hawkins, and R. W. Boswell. Particle in cell simulation of a radiofrequency plasma jet expanding in vacuum. *Applied Physics Letters*, 106(9):093502, 2015. ISSN 0003-6951. doi:10.1063/1.4914109.

[25] C. Charles, R. W. Boswell, A. Bish, V. Khayms, and E. F. Scholz. Direct Measurement of Axial Momentum Imparted by an Electrothermal Radiofrequency Plasma Micro-Thruster. *Frontiers in Physics*, 4(May):1–6, 2016. ISSN 2296-424X. doi:10.3389/fphy.2016.00019.

[26] A. Fruchtman, G. Makrinich, P. Chabert, and J. M. Rax. Enhanced plasma transport due to neutral depletion. *Physical Review Letters*, 95(11):1–4, 2005. ISSN 00319007. doi:10.1103/PhysRevLett.95.115002.

[27] J. L. Raimbault, L. Liard, J. M. Rax, P. Chabert, A. Fruchtman, and G. Makrinich. Steady-state isothermal bounded plasma with neutral dynamics. *Physics of Plasmas*, 14(1), 2007. ISSN 1070664X. doi:10.1063/1.2424558.

[28] L. Liard, J. L. Raimbault, J. M. Rax, and P. Chabert. Plasma transport under neutral gas depletion conditions. *Journal of Physics D: Applied Physics*, 40(17):5192–5195, 2007. ISSN 00223727. doi:10.1088/0022-3727/40/17/026.

[29] A. Fruchtman. Energizing and depletion of neutrals by a collisional plasma. *Plasma Sources Science and Technology*, 17(2), 2008. ISSN 09630252. doi:10.1088/0963-0252/17/2/024016.

[30] P. Chabert and N. Braithwaite. *Physics of Radio-Frequency Plasmas*. Cambridge University Press, Cambridge, 3rd edition, 2014.

[31] J. Schulze, Z. Donkó, D. Luggenhölscher, and U. Czarnetzki. Different modes of electron heating in dual-frequency capacitively coupled radio frequency discharges. *Plasma Sources Science and Technology*, 18:034011, 2009. ISSN 0963-0252. doi:10.1088/0963-0252/18/3/034011.

[32] J. Schulze, A. Derzsi, K. Dittmann, T. Hemke, J. Meichsner, and Z. Donkó. Ionization by drift and ambipolar electric fields in electronegative capacitive radio frequency plasmas. *Physical Review Letters*, 107(27):1–5, 2011. ISSN 00319007. doi:10.1103/PhysRevLett.107.275001.

[33] M.A. Lieberman. Analytical solution for capacitive RF sheath. *IEEE Transactions on Plasma Science*, 16(6): 638–644, 1988. ISSN 00933813. doi:10.1109/27.16552.

[34] J. Schulze, B. G. Heil, D. Luggenhölscher, R. P. Brinkmann, U. Czarnetzki, and D. Luggenh. Stochastic heating in asymmetric capacitively coupled RF discharges. *Journal of Physics D: Applied Physics*, 41(19):195212, 2008. ISSN 0022-3727. doi:10.1088/0022-3727/41/19/195212.

[35] K. H. Schoenbach, A. El-habachi, W. Shi, and M. Ciocca. High-pressure hollow cathode discharges. *Plasma Sources Science and Technology*, 6:468–477, 1997. doi:10.1088/0963-0252/6/4/003.

[36] A. V. Phelps and Z. Lj. Petrovic. Cold-cathode discharges and breakdown in argon: surface and gas phase production of secondary electrons. *Plasma Sources Science and Technology*, 8(3):R21–R44, 1999. ISSN 0963-0252. doi:10.1088/0963-0252/8/3/201.

[37] T. Lafleur, R. W. Boswell, and J.-P. Booth. Enhanced sheath heating in capacitively coupled discharges due to non-sinusoidal voltage waveforms. *Applied Physics Letters*, 100(19), 2012. ISSN 00036951. doi:10.1063/1.4712128.

[38] S. J. Doyle, T. Lafleur, A. R. Gibson, P. Tian, M. J. Kushner, and J. Dedrick. Enhanced control of the ionization rate in radio-frequency plasmas with structured electrodes via tailored voltage waveforms. 26:125005, 2017. doi:10.1088/1361-6595/aa96e5.

[39] T. Lafleur, P. A. Delattre, J. P. Booth, E. V. Johnson, and S. Dine. Radio frequency current-voltage probe for impedance and power measurements in multi-frequency unmatched loads. *Review of Scientific Instruments*, 84(1), 2013. ISSN 00346748. doi:10.1063/1.4773540.

[40] V. A. Godyak and R. B. Piejak. Insitu simultaneous radio frequency discharge power measurements. *Journal of Vacuum Science & Technology A: Vacuum, Surfaces, and Films*, 8(5):3833–3837, 1990. ISSN 0734-2101. doi:10.1116/1.576457.

[41] D. Marinov and N. St J. Braithwaite. Power coupling and electrical characterization of a radio-frequency micro atmospheric pressure plasma jet. *Plasma Sources Science and Technology*, 23(6):3–9, 2014. ISSN 13616595. doi:10.1088/0963-0252/23/6/062005.

[42] T Gans, C C Lin, V Schulz-von der Gathen, and H F Döbele. Phase-resolved emission spectroscopy of a hydrogen rf discharge for the determination of quenching coefficients. *Phys. Rev. A*, 67:12707, 2003. ISSN 1050-2947. doi:10.1103/PhysRevA.67.012707.

[43] T. Gans, D. O'Connell, V. Schulz-von der Gathen, and J. Waskoenig. The challenge of revealing and tailoring the dynamics of radio-frequency plasmas. *Plasma Sources Science and Technology*, 19(3):034010, 2010. ISSN 0963-0252. doi:10.1088/0963-0252/19/3/034010.

[44] S. Siepa and U. Czarnetzki. Line integration and spatial resolution in optical imaging of plasmas. *Journal of Physics D: Applied Physics*, 48:385201, 2015. doi:10.1088/0022-3727/48/38/385201.

[45] J. Schulze, E. Schüngel, Z. Donkó, D. Luggenhölscher, and U. Czarnetzki. Phase resolved optical emission spectroscopy: a non-intrusive diagnostic to study electron dynamics in capacitive radio frequency discharges. *Journal of Physics D: Applied Physics*, 43(12):124016, 2010. ISSN 0022-3727. doi:10.1088/0022-3727/43/12/124016.

[46] J. E. Chilton, J. B. Boffard, R. S Schappe, and C. C. Lin. Measurement of electron-impact excitation into the $3p^5 4p$ levels of argon using Fourier-transform spectroscopy. *Physical Review A*, 57(1):267–277, 1998. ISSN 1050-2947. doi:10.1103/PhysRevA.57.267.

[47] K. Niemi, S. Reuter, L. M. Graham, J. Waskoenig, N. Knake, V. Schulz-Von Der Gathen, and T. Gans. Diagnostic based modelling of radio-frequency driven atmospheric pressure plasmas. *Journal of Physics D: Applied Physics*, 43(12), 2010. ISSN 00223727. doi:10.1088/0022-3727/43/12/124006.

[48] R. H. Huddlestone and S. L. Leonard. *Plasma Diagnostic Techniques.pdf*. Academic Press, New York, 1965.

[49] A. Anders. *A Formulary for Plasma Physics*. Akademie-Verlag, Berlin, 1990. ISBN 3055012631.

[50] N. Sadeghi, D. W. Setser, A. Francis, U. Czarnetzki, and H. F. Döbele. Quenching rate constants for reactions of $Ar(4p[1/2]_{0'}$, $4p[1/2]_{0'}$, $4p[3/2]_{2'}$, and $4p[5/2]_2)$ atoms with 22 reagent gases. *Journal of Chemical Physics*, 115(7): 3144–3154, 2001. ISSN 00219606. doi:10.1063/1.1388037.

[51] M. J. Kushner. Hybrid modelling of low temperature plasmas for fundamental investigations and equipment design. *Journal of Physics D: Applied Physics*, 42(19):194013, 2009. ISSN 0022-3727. doi:10.1088/0022-3727/42/19/194013.

[52] P. Tian and M. J. Kushner. Controlling VUV photon fluxes in low-pressure inductively coupled plasmas. *Plasma Sources Science and Technology*, 24:34017, 2015. ISSN 0963-0252. doi:10.1088/0963-0252/24/3/034017.

[53] M. A. Furman and M. T. F. Pivi. Probabilistic model for the simulation of secondary electron emission. *Physical Review Special Topics - Accelerators and Beams*, 5(12):82–99, 2002. ISSN 10984402. doi:10.1103/PhysRevSTAB.5.124404.

[54] S.-H. Song and M. J. Kushner. Control of electron energy distributions and plasma characteristics of dual frequency, pulsed capacitively coupled plasmas sustained in Ar and Ar/CF4/O2. *Plasma Sources Science and Technology*, 21 (5):55028, 2012. ISSN 0734-2101. doi:10.1088/0963-0252/21/5/055028.

[55] D. L. Scharfetter and H. K. Gummel. Large-Signal Analysis of a Silicon Read Diode Oscillator. *IEEE Transactions on Electron Devices*, 16(1):64–77, 1969. ISSN 15579646. doi:10.1109/T-ED.1969.16566.

[56] M. Hayashi. Report No. IPPJ-AM-19. Technical report, Nagoya Institute of Technology, 1991.

[57] K. Tachibana. Excitation of the $1s_5$, $1s_4$, $1s_3$ and $1s_2$ levels of argon by low-energy electrons. *Physical Review A*, 34(2), 1986. doi:10.1103/PhysRevA.34.1007.

[58] D. Rapp and P. EnglanderGolden. Total Cross Sections for Ionization and Attachment in Gases by Electron Impact. I. Positive Ionization. *The Journal of Chemical Physics*, 43(5):1464–1479, 1965. ISSN 0021-9606. doi:10.1063/1.1696957.

[59] N. A. Dyatko, Y. Z. Ionikh, I. V. Kochetov, D. L. Marinov, A. V. Meshchanov, A. P. Napartovich, F. B. Petrov, and S. A. Starostin. Experimental and theoretical study of the transition between diffuse and contracted. *J. Phys. D: Appl. Phys*, 41:055204, 2008. doi:10.1088/0022-3727/41/5/055204.

[60] A. Bogaerts, R. G. V. Serikov, and V. V. Serikov. Calculation of gas heating in direct current argon glow discharges. *Journal of Applied Physics*, 87, 1999. doi:10.1063/1.373545.

[61] H. W. Ellis, R. Y. Pai, E. W. McDaniel, E. A. Mason, and L. A. Viehland. Transport Properties of Gaseous Ions Over a Wide Energy Range. *Atomic Data and Nuclear Data Tables*, 17(3):177–210, 1976. doi:10.1016/0092-640X(76)90001-2.

[62] A. R. Gibson, M. Foucher, D. Marinov, P. Chabert, T. Gans, M. J. Kushner, and J.-P. Booth. The role of thermal energy accommodation and atomic recombination probabilities in low pressure oxygen plasmas. *Plasma Physics and Controlled Fusion*, 59:024004, 2017. doi:10.1088/1361-6587/59/2/024004.

[63] A. J. Lofthouse, L. C. Scalabrin, and I. D. Boyd. Velocity Slip and Temperature Jump in Hypersonic Aerothermodynamics. *Journal of Thermophysics and Heat Transfer*, 22(1):38–49, 2008. ISSN 0887-8722. doi:10.2514/1.31280.

[64] H. Yamaguchi, K. Kanazawa, Y. Matsuda, T. Niimi, A. Polikarpov, and I. Graur. Investigation on heat transfer between two coaxial cylinders for measurement of thermal accommodation coefficient. *Physics of Fluids*, 24(6), 2012. ISSN 10706631. doi:10.1063/1.4726059.

[65] W. M. Trott, J. N. Castaeda, J. R. Torczynski, M. A. Gallis, and D. J. Rader. An experimental assembly for precise measurement of thermal accommodation coefficients. *Review of Scientific Instruments*, 82(3), 2011. ISSN 00346748. doi:10.1063/1.3571269.

[66] W. Steckelmacher. Knudsen flow 75 years on: The current state of the art for flow of rarefied gases in tubes and systems. *Reports on Progress in Physics*, 49(10):1083–1107, 1986. ISSN 00344885. doi:10.1088/0034-4885/49/10/001.

[67] X. Chen and E. Pfender. Effect of the Knudsen number on heat transfer to a particle immersed into a thermal plasma. *Plasma Chemistry and Plasma Processing*, 3(1):97–113, 1983. ISSN 02724324. doi:10.1007/BF00566030.

[68] P. A. Thompson. *Compressible Fluid Dynamics*. McGraw-Hill, New York, 2nd edition, 1994. ISBN 9780070644052.

[69] L. Wu. A slip model for rarefied gas flows at arbitrary Knudsen number. *Applied Physics Letters*, 93(25):2006–2009, 2008. ISSN 00036951. doi:10.1063/1.3052923.

[70] R. A. Arakoni, J. J. Ewing, and M. J. Kushner. Microdischarges for use as microthrusters: modelling and scaling. *Journal of Physics D: Applied Physics*, 41(10):105208, 2008. ISSN 0022-3727. doi:10.1088/0022-3727/41/10/105208.

[71] L Garrigues and P Coche. Electric propulsion: comparisons between different concepts. *Plasma Physics and Controlled Fusion*, 53(12):124011, 2011. ISSN 0741-3335. doi:10.1088/0741-3335/53/12/124011.

[72] Stéphane Mazouffre. Electric propulsion for satellites and spacecraft: established technologies and novel approaches. *Plasma Sources Science and Technology*, 25(3):033002, 2016. ISSN 0963-0252. doi:10.1088/0963-0252/25/3/033002.

[73] Teck Seng Ho, Christine Charles, and Rod Boswell. Performance modelling of plasma microthruster nozzles in vacuum. *Journal of Applied Physics*, 123(17):173301, 2018. ISSN 0021-8979. doi:10.1063/1.5012765.

[74] S. Dixon, C. Charles, J. Dedrick, T. Gans, D. O'Connell, and R. Boswell. Observations of a mode transition in a hydrogen hollow cathode discharge using phase resolved optical emission spectroscopy. *Applied Physics Letters*, 105 (1), 2014. ISSN 00036951. doi:10.1063/1.4889916.

[75] M. A. Lieberman and A. J. Lichtenberg. *Principles of Plasma Discharges and Materials Processing*. John Wiley & Sons, New Jersey, 2nd edition, 2005. ISBN 0-471-72001-1. doi:10.1017/CBO9781107415324.004.

[76] T. Lafleur, P. Chabert, and J.-P. Booth. Secondary electron induced asymmetry in capacitively coupled plasmas. *Journal of Physics D: Applied Physics*, 46(13):135201, 2013. ISSN 0022-3727. doi:10.1088/0022-3727/46/13/135201.

[77] A. Derzsi, I. Korolov, E. Schüngel, Z. Donkó, and J. Schulze. Effects of fast atoms and energy-dependent secondary electron emission yields in PIC/MCC simulations of capacitively coupled plasmas. *Plasma Sources Science and Technology*, 24(3), 2015. ISSN 13616595. doi:10.1088/0963-0252/24/3/034002.

[78] M. Daksha, A. Derzsi, S. Wilczek, J. Trieschmann, T. Mussenbrock, P. Awakowicz, Z. Donkó, and J. Schulze. The effect of realistic heavy particle induced secondary electron emission coef fi cients on the electron power absorption dynamics in single- and dual-frequency capacitively coupled plasmas. *Plasma Sources Science and Technology*, 26: 085006, 2017. doi:10.1088/1361-6595/aa7c88.

[79] C. M. O. Mahony, R. Al Wazzan, and W. G. Graham. Sheath dynamics observed in a 13.56 MHz-driven plasma. *Applied Physics Letters*, 71(5):608, 1997. ISSN 00036951. doi:10.1063/1.119808.

[80] T. Lafleur. Tailored-waveform excitation of capacitively coupled plasmas and the electrical asymmetry effect. *Plasma Sources Science and Technology*, 25(1):013001, 2016. ISSN 0963-0252. doi:10.1088/0963-0252/25/1/013001.

[81] K. R. Williams, K. Gupta, and M. Wasilik. Etch Rates for Micromachining Processing II. *Journal of Microelectromechanical systems*, 12(6):761–777, 2003. ISSN 1098-6596. doi:10.1017/CBO9781107415324.004.

[82] A. Benninghoven, F.G. Rudenauer, and H.W. Werner. *Secondary ion mass spectrometry: basic concepts, instrumental aspects, applications and trends*. Wiley and Sons, Cambridge, 1st edition, 1 1987. doi:10.1002/sia.740100811.

[83] J. Schulze, E. Schüngel, Z. Donkó, and U. Czarnetzki. Charge dynamics in capacitively coupled radio frequency discharges. *Journal of Physics D: Applied Physics*, 43:225201, 2010. ISSN 0022-3727. doi:10.1088/0022-3727/43/22/225201.